

pubs.acs.org/Macromolecules Article

Structure, Dynamics, and Rheology of Vitrimers

Jianshe Xia, Julia Ann Kalow, and Monica Olvera de la Cruz*



Cite This: Macromolecules 2023, 56, 8080-8093



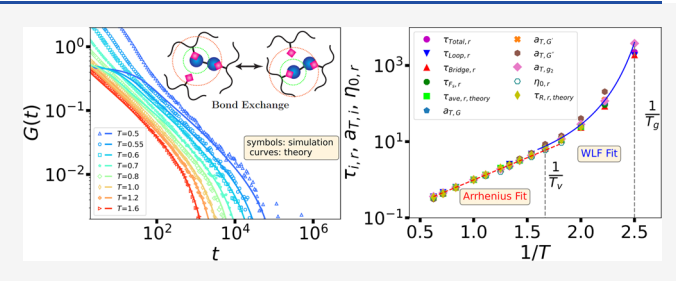
ACCESS I

Metrics & More

Article Recommendations

Supporting Information

ABSTRACT: Vitrimers are associative covalent adaptable networks that undergo reversible bond-exchange reactions while maintaining a fixed cross-linking density with changing temperature. To date, experimental studies that rely on macroscopic rheology have not been able to reveal topological changes and microscopic dynamics in these materials. Here, coarse-grained molecular dynamics simulations combined with a Monte Carlo method are implemented to investigate the topological structural changes, microscopic dynamics, and linear rheology of unentangled



side-chain-linked vitrimers in conjunction with the sticky Rouse model (SRM). We find that there is a minor variation in the topological structure with temperature. The dynamic heterogeneities of the bond-exchange behavior and the system dynamics increase remarkably when approaching the topological freezing transition temperature T_{ν} . Quantitative agreement between the simulation results and the SRM predictions is observed for the stress relaxation, elastic and loss moduli, and the relative mean-squared displacement, especially at the intermediate- and long-time or low-frequency regimes, where the time-temperature superposition principle is satisfied. We obtain a scaling collapse curve for the dynamic bond relaxation time, the zero-shear viscosity, and the horizontal shift factors without introducing any parameters, suggesting that the microscopic and macroscopic dynamics exhibit a similar relaxation behavior even in the presence of loop defects. Moreover, these results are in good agreement with those predicted by the SRM, indicating that the linear rheology of unentangled vitrimers with a fast bond-exchange rate can be analyzed via a single-chain approach based on the SRM.

INTRODUCTION

Thermosetting polymeric materials, which are composed of three-dimensional cross-linked networks, are ubiquitous and widely applied in everyday life due to their exceptional thermal, chemical, and dimensional stability and resistance to solvent and environmental stress.^{1,2} However, the presence of permanent and irreversible cross-linking bonds among the polymer chains in thermosets prevents flow via bond exchange, 2,3 required for reprocessing and self-healing. Thus, conventional thermosetting materials must be discarded after damage or fracture during service, leading to environmental pollution.³ To tackle this problem, the permanent cross-links have been replaced with reversible associative interactions. For example, noncovalent bonds such as hydrogen bonds, $^{4,5}\pi-\pi$ stacking,⁶ and metal-ligand bonds⁷ were introduced as crosslinkers to thermosetting matrices, forming what is referred to as transient or physical associative polymer networks. Compared to permanent cross-linking covalent bonds, these transient bonds can be reversibly broken and reformed under thermal fluctuation or an external stimulus, imparting thermosetting materials with recyclable and self-healing properties.^{8,9} However, these noncovalent bonds can lead to weaker mechanical properties than conventional thermosetting materials due to their lower bonding energies (1–5 kcal/mol) compared with the covalent bond energy of typically 50-150 kcal/mol. 10,11 In the past two decades, a new paradigm

covalent adaptable network (CAN) has been proposed in thermosetting materials, where the cross-links are exchangeable covalent bonds, helpful to the self-healing, shape memory, and recycling of thermosets. According to the different exchange mechanism of the covalent bond, they can be further classified into dissociative and associative covalent adaptable networks (DCANs and ACANs), of which ACANs are also referred to as vitrimers. 18,19

In DCANs, the cross-linking bonds first break apart and then reconstruct after some time. As more dynamic bonds are activated, there is a remarkable change in the macromolecular structure due to the loss of cross-links. ^{20,21} For example, Adzima et al. investigated a covalently cross-linked polymer network based on a Diels—Alder (DA) reaction, where significant depolymerization occurred at high temperatures via the retro-DA reaction, and with decreasing temperature, the rate of DA reaction increased and the material went through a liquid-like to solid-like transition, that is, gelation conversion. Furthermore, based on the Winter—Chambon gel-point

Received: July 10, 2023
Revised: August 23, 2023
Published: September 29, 2023





criterion,²² that is, the elastic and loss moduli follow similar frequency scaling at the gel-point conversion, the gel-point temperature of the materials was determined and consistent with the predicted value by the Flory-Stockmayer equation, indicating that the Winter-Chambon gel-point criterion is valid for DCANs. By contrast, the breaking and reformation of the cross-links in vitrimers happen concurrently, resulting in a minimal change in the macromolecular structure and a fixed cross-linking density during bond exchange.²³ Since the seminal report of Leibler et al. 16 on ACANs based on transesterification reactions, various exchange reactions have been designed and implemented for the preparation of vitrimeric materials. ^{18,19,23,24} Ishibashi and Kalow²⁵ designed a vitrimeric silicone elastomer exploiting the uncatalyzed reversible conjugate addition-elimination reaction. They found that after 10 remolding cycles, there was no evident erosion of mechanical properties for these new elastomers. The rate of cross-link reconfiguration can be tuned using the structure of the conjugate acceptor.²⁶ These materials are suitable model systems because of their tunability, robustness, and absence of a catalyst.

Vitrimers usually have two characteristic transition temperatures, that is, the conventional glass-transition temperature T_{σ} and the topology freezing transition temperature T_{ν} , where T_{g} represents the transition from the glassy to the rubbery state and T_v is utilized to identify the viscoelastic phase transition from the rubbery state to the viscous liquid. In most vitrimers, T_{ν} is greater than $T_{\rm g}$. At temperatures lower than T_{ν} vitrimers exhibit a solid-like behavior. Above T_{ν} they will flow like viscoelastic liquids due to the topological rearrangement enabled by the dynamic bond exchange. The viscoelastic behavior is considered to be dictated by the exchange rate of the dynamic bond, in line with the observed Arrhenius-type behavior. Therefore, T_{ν} is of vital importance for determining the application and remolding of vitrimers. In their pioneering report, Leibler and co-workers defined T_{ν} as the temperature at which the viscosity becomes higher than 10¹² Pa·s, based on the conventional definition for glasses. However, as pointed out in an earlier work, 29 T_{ν} is commonly determined by extrapolating viscosity into regions where viscosity may follow different temperature dependence due to the influence of various factors at low temperatures. Recently, Fang et al.³⁰ reported that the normalized relaxation modulus exhibited frequency-independent behavior and followed a power-law relationship over a temperature interval by investigating epoxy vitrimers. They called the critical transition a solid-solid transition and the corresponding transition temperature as T_{ν} . In simulations, Perego et al. 31,32 defined T_{ν} based on the local minimum of the thermal expansion coefficient as a function of temperature by applying coarse-grained (CG) molecular dynamics (MD) simulations in combination with a Monte Carlo (MC) method. Additionally, they found that T_v could also be defined by the temperature dependence of the microscopic relaxation time and the shift factor a_T used to rescale the rheological data. By comparing the viscoelastic behaviors of the end-linked vitrimer and thermoset, they found that the horizontal shift factor a_T could be well described by a WLF equation for the thermoset. For vitrimers, a_T followed a combination of the Arrhenius and WLF-like behavior above and below T_{ν} . As a result, the dynamic bond reactions are helpful for the dynamic relaxation of systems and lead to an Arrhenius-type relaxation behavior.

Due to the presence of associative bond exchange, vitrimers commonly possess unusual rheological behavior compared to conventional thermosetting materials. To date, linear rheology studies on vitrimers have been widely carried out by experiments 10,30,33 and simulations. 31,32,34,35 Meng et al. 33 explored the rheology of vitrimers through a combination of experiments and theories and proposed different methods to characterize material parameters based on the rheological data. Fang et al.³⁰ investigated the linear viscoelasticity of the curing and cured epoxy vitrimer and surprisingly found that after being fully cured, the material at T_{ν} exhibited the behavior of a critical gel. Tang et al.35 studied the discrepancies and limits of viscoelasticities between DCANs and ACANs by using a hybrid MD-MC simulation. Given that the cross-linking covalent bonds are dynamic and transient in vitrimers, Ricarte et al.³⁴ extended the sticky Rouse model (SRM), which was originally aimed at the transient polymer networks by introducing an effective friction coefficient to the Rouse model,^{36,37} to unentangled vitrimers to elucidate the relationships between structure and viscoelasticity of unentangled vitrimer melts by theoretical calculations. However, the validity and effectiveness of the SRM in predicting the linear rheology of unentangled vitrimers remain to be further evaluated.

To investigate the complex structure, dynamics, and viscoelastic behavior of vitrimers at a molecular level, various simulation methods have been put forward. Sciortino et al.³⁸ proposed the method of a three-body potential for modeling bond-exchange dynamics in molecular dynamics simulation. Using the model, they investigated self- and collective dynamics, the effect of topological defects on stress relaxation, self-adhesion, and healing of vitrimers as well as explored the fragility of vitrimeric polymers.^{39–42} Liu et al.⁴³ examined the energy barrier of bond exchange on various mechanical properties of vitrimers and indicated that an intermediate value of the energy barrier was helpful for the best mechanical performance. Although the method is able to effectively reproduce the bond-exchange process, it is greatly influenced by thermal fluctuations or external forces, considering that the dynamic bond is described by a nonbonded Lennard-Jones (LJ) potential.⁴⁴ In the past decade, many hybrid MD-MC algorithms have been proposed to investigate physical associative polymer networks by adopting a bond potential to describe the associating interaction among polymer chains. 45-47 For example, Hoy and Fredrickson 46 used hybrid MD/MC simulations to study thermodynamics, chemical kinetics, and mechanical properties of physical associative polymers. As mentioned before, the cross-linking density in vitrimers is fixed during the bond exchange and is independent of temperature, which is significantly different from physical associating polymer networks where the number of sticky bonds is considerably affected by temperature and sticky energy, leading to significant changes in the topological structures.46 Consequently, modified hybrid MD-MC algorithms have been widely applied to simulate the explicit bond exchange in vitrimers. 32,35,44,48 Based on the method, Perego et al. 31,32 successfully captured two transition temperatures (T_{σ} and T_{ν}) and explored the connection between the microscopic molecular dynamics and the linear viscoelastic properties for end-linked vitrimers using the generalized Stokes-Einstein equation. Wu et al.44 showed that the bond-exchange rate changed the diffusion mode of molecules, thus affecting the relaxation dynamics of vitrimers.

In this paper, we investigate the topological structure changes and determine the microscopic dynamics and linear viscoelastic behaviors of unentangled side-chain-linked vitrimers by combining hybrid MD-MC simulations with the SRM. As mentioned above, DCANs tend to exhibit a gelation conversion with decreasing temperature, but it seems difficult to detect such a similar phase transition in experiments when approaching T_{v} for vitrimers due to the fixed cross-linking density at all temperatures.¹³ Therefore, we explore whether there exists a similar gelation transition near T_v via hybrid MD and MC methods for side-chain-linked vitrimers. The simulated system is based on the experimental vitrimeric silicone elastomer (polydimethylsiloxane, PDMS) from the Kalow group. 25 The organization of the paper is as follows. We first describe the SRM, the simulation method, and computational details. We then analyze the changes in topological structures and identify the glass-transition temperature and the topological freezing transition temperature, followed by calculating the dynamic heterogeneity and linear rheology. We then compare the simulated results and the SRM predictions for the linear viscoelasticity and examine the time-temperature superposition (TTS) principle via simulations. Finally, a detailed discussion and conclusion are provided.

MODEL AND METHOD

Sticky Rouse Model. As mentioned in the introduction, the cross-linking density of vitrimers is conserved at different temperatures and the cross-link is a dynamic covalent bond instead of a noncovalent bond comprising particle clusters with different sizes as described by a previous work.³⁷ Thus, the SRM should be suitable to describe the relaxation of unentangled vitrimers. In the SRM, the beads involved in the transient cross-links, that is, sticky beads, are considered to have a larger friction coefficient than regular beads due to their longer lifetime so that the linear rheological properties of vitrimers can be analyzed via a single-chain approach. For an unentangled Gaussian bead spring chain consisting of N beads, of which n_s beads are sticky, the motion equation of the beads can be expressed as

$$\dot{\mathbf{R}}_{i} = -\frac{k}{\zeta_{i}} (2\mathbf{R}_{i} - \mathbf{R}_{i+1} - \mathbf{R}_{i-1}) + \mathbf{f}_{i}, i = 2, 3, ..., N - 1$$
(1)

where \mathbf{R}_i is the position of particle i. The spring constant $k=3k_{\rm B}T/b^2$, where $k_{\rm B}$ is the Boltzmann constant and b is the Kuhn length; ζ_i is the friction coefficient acting on particle i with $\zeta_i=\zeta_s$ if the particle is a sticky bead, otherwise $\zeta_i=\zeta_s$; and \mathbf{f}_i is the random force acting on the bead i, satisfying the fluctuation—dissipation theorem. Considering the chain connectivity, eq 1 can be further modified as the spring motion equation

$$\dot{\mathbf{r}}_i + \sum_{j=1}^{N-1} C_{ij} \mathbf{r}_j = \mathbf{f}_i, \ i = 1, 2, ..., N-1$$
(2)

where the spring vector $\mathbf{r}_i = \mathbf{R}_{i+1} - \mathbf{R}_i$. The matrix \mathbf{C} describes the connectivity of the springs. We can define a relative effective friction coefficient as $\delta = \frac{\zeta_i}{\zeta}$ for sticky beads. For a linear chain, \mathbf{C} is a tridiagonal matrix and $C_{ij} = (k/\zeta)A_{ij}$, where

$$A_{i,i-1} = -1/\delta_i$$

$$A_{i,i} = 1/\delta_i + 1/\delta_{i+1}$$

$$A_{i,i+1} = -1/\delta_{i+1}$$
(3)

 $\delta_i = \delta$ if bead i is a sticky bead; otherwise, $\delta_i = 1$. By calculating the matrix \mathbf{A} , the stress relaxation time τ_i can be directly obtained, that is, $\tau_i = \frac{\tau_0}{2\lambda_i}$, where $\tau_0 = \frac{b^2}{3k_{\mathrm{B}}T}\zeta$ and λ_i is the eigenvalue of the matrix \mathbf{A} , from which the linear relaxation modulus is expressed as

$$G(t) = \frac{\rho k_{\rm B} T}{N} \sum_{i=1}^{N-1} \exp\left(-\frac{t}{\tau_i}\right) \tag{4}$$

where ρ is the number density of beads. The elastic and loss moduli in the space of frequency ω are also separately given by

$$G'(\omega) = \frac{\rho k_{\rm B} T}{N} \sum_{i=1}^{N-1} \frac{(\omega \tau_i)^2}{1 + (\omega \tau_i)^2}$$
(5)

$$G''(\omega) = \frac{\rho k_{\rm B} T}{N} \sum_{i=1}^{N-1} \frac{\omega \tau_i}{1 + (\omega \tau_i)^2}$$
(6)

The zero-shear viscosity and the average relaxation time are obtained by

$$\eta_0 = \frac{\rho k_{\rm B} T}{N} \sum_{i=1}^{N-1} \tau_i \tag{7}$$

$$\tau_{\text{ave}} = \frac{1}{N} \sum_{i=1}^{N-1} \tau_i$$
 (8)

Equation 1 can be also rewritten into a group of independent equations by introducing the normal coordinates \mathbf{X}_p

$$\dot{\mathbf{X}}_{p} = -\frac{k\lambda_{p}}{\zeta_{p}}\mathbf{X}_{p} + \mathbf{f}_{p}, p = 0, 1, ..., N - 1$$
 (9)

where $\lambda_0 = 0$, and λ_p (p > 0) is the eigenvalue of the matrix **A**. The position of particle *i* can also be represented by the inverse transformation of normal coordinates \mathbf{X}_n^{37}

$$\mathbf{R}_{i} = \sum_{i=1}^{i=N} \zeta_{i} \mathbf{R}_{i} / \sum_{i=1}^{N} \zeta_{i} + \sum_{p=1}^{N-1} v_{i}^{p} \mathbf{X}_{p}$$
(10)

where v_i^p is the *i*th element of the *p*th eigenvector of the matrix \mathbf{A} and $\sum_{i=1}^{i=N} \zeta_i \mathbf{R}_i / \sum_{i=1}^N \zeta_i$ can be regarded as the chain effective center of mass $\mathbf{r}_{\text{cm/eff}}$. Therefore, similar to the classic Rouse model, the linear viscoelastic quantities can be directly obtained by identifying the relative effective friction coefficients of the sticky beads for unentangled vitrimers.

Simulation Method. We employ the Kremer–Grest bead spring (KGBS) model, ⁴⁹ which is widely used for modeling linear and cross-linking polymers, ^{50,51} to construct the vitrimeric system without considering the bond angular potential. In terms of the vitrimeric silicone elastomer developed experimentally, ²⁵ a branched polymer system with 800 chains is considered, where each chain has 40 beads in the backbone smaller than the entanglement length $50 \le N_e \le 85$ of the KGBS model ^{52,53} and is randomly grafted by reactive beads denoted as A with the average value of $N_A = 6$. To create

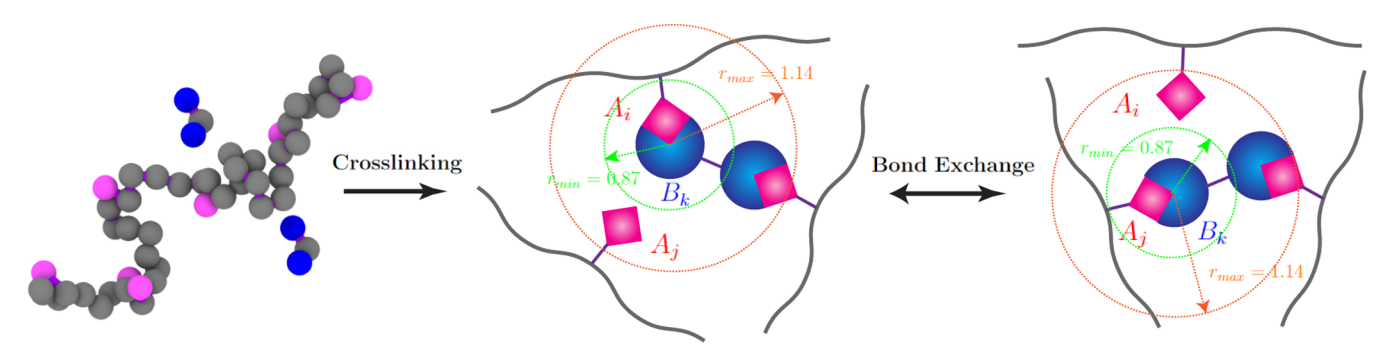


Figure 1. Schematic diagrams of the cross-linking and bond-exchange reactions between the branched polymer chain and the cross-linker. The red bead represents the reactive A bead in the branched chain. The gray bead is the regular bead. The blue bead represents the reactive B bead in the two-functional cross-linker consisting of three beads, where the regular bead is not shown in the right plots. When a free reactive bead A_j is in the range $(r_{\min} \le r \le r_{\max})$ of a reactive bead B_k bonded with A_p a bond-exchange reaction will occur with a probability determined by the total energy change.

the grafted A beads, each bead along the backbone is checked by comparing a random number between 0 and 1 with constant probability $p_s = 6/40$. If the random number is larger than p_s , a reactive A bead will be created and grafted in the corresponding bead of the backbone; otherwise, the A bead will not be created. We carry out multiple iterations to ensure that the average number of A-type beads per chain is 6, that is, $N_A = 6$. Considering the chemical reaction mechanism of the bond exchange²⁵ and the cross-linking density should be above the gel point, the branched polymer system is mixed with 1600 two-functional cross-linkers consisting of three beads where two-end beads denoted by B are reactive. In the simulation system, only A and B beads can form the exchangeable covalent bonds, and these A beads connected with B beads are regarded as sticky beads according to the SRM, as shown in Figure 1. The truncated and shifted LJ potential and the finitely extensible nonlinear elastic (FENE) potential⁴⁹ are adopted to describe the nonbonded and bonded interaction of beads, respectively.

$$U_{LJ}(r) = \begin{cases} 4\epsilon \left[\left(\frac{\sigma}{r} \right)^{12} - \left(\frac{\sigma}{r} \right)^{6} - \left(\frac{\sigma}{r_{c}} \right)^{12} + \left(\frac{\sigma}{r_{c}} \right)^{6} \right] & \text{if } r \leq r_{c} \\ 0 & \text{if } r > r_{c} \end{cases}$$

$$U_{\text{Bond}}(r) = -\frac{1}{2}KR_0^2 \ln \left[1 - \left(\frac{r}{R_0}\right)^2\right]$$
 (12)

where the cutoff radius $r_c=1.5\sigma$ is used for improving the computational efficiency. The maximum bond length $R_0=1.5\sigma$ and the spring constant $K=30\epsilon/\sigma$ are applied for the permanent and exchangeable covalent bonds. All quantities in the simulations are in units of the LJ bead diameter σ , interbead interaction energy ϵ , and time $\tau_{\rm LJ}=\sqrt{m\sigma^2/\epsilon}$, where m is an LJ bead mass. The initial mixture is relaxed in a canonical ensemble (NVT) for 10^7 steps with periodic boundary conditions and the Langevin thermostat and gradually compressed until the system number density $\rho=0.85/\sigma^3$. The dense packing chains are cross-linked by the cross-linkers until there is no unpaired B bead, where each A or B bead can additionally bond with only one B or A bead. A full vulcanization-like network is generated with some topological defects such as loops, analogous to the real polymer networks.

All of the simulations are performed in the LAMMPS^{S4} software package. The motion equation of beads is integrated using the Verlet algorithm with a time step of $\delta t = 0.01 \tau_{\rm LJ}$, and the simulated temperature T is from 0.1 to 2.0 $\epsilon/k_{\rm B}$.

Inspired by previous works, 31,44 a similar hybrid MD-MC simulation method is applied, where the beads move based on the MD motion equations and the bond exchange is performed in an MC step. The MC steps occur at every 10 MD steps, that is, the MC time-step size, $\tau_{\rm MC} = 0.1\tau_{\rm LJ}$. As indicated by previous works, 45,46 a small $\tau_{\rm MC}$ is helpful to reduce the statistical error and obtain good statistics. However, the change in the $\tau_{\rm MC}$ value does not affect the qualitative results and conclusions obtained in the equilibrium systems. Thus, we choose a relatively small MC time step. All of the A and B beads are sampled at each MC step. For example, as depicted in Figure 1, when a free reactive bead A_j is in the range $(0.87 \le r \le 1.14)$ of a reactive bead B_k bonded with A_n a bond-exchange reaction will probably occur

$$A_i - B_k + A_j \rightleftharpoons A_j - B_k + A_i \tag{13}$$

depending on the total energy change $\Delta U_{\mathrm{change}}$, which is given by

$$\Delta U_{\text{change}} = U_{LJ}(A_i, B_k) + U_{\text{Bond}}(A_j, B_k) - U_{LJ}(A_j, B_k) - U_{\text{Bond}}(A_i, B_k)$$

$$(14)$$

where $U_{\rm Bond}(A_i, B_k)$ and $U_{\rm LJ}(A_i, B_k)$ are, respectively, the bonded and nonbonded interaction energies between A_i and B_k before and after the bond-exchange reaction, and $U_{\rm LJ}(A_j, B_k)$ and $U_{\rm Bond}(A_j, B_k)$ are, respectively, the nonbonded and bonded interaction energies between A_j and B_k before and after the bond-exchange reaction. The reaction range is determined by the distribution of the bond length described by the FENE potential, 44 thus avoiding remarkable disturbances to the system. If $\Delta U_{\rm change} \leq 0$, the proposed move is obviously accepted; otherwise, the acceptance of the move is determined by the probability in terms of the Metropolis acceptance criterion. Such a reaction rule can ensure the constant cross-linking density of the system during the simulation and satisfy the detailed balance.

Due to the constant cross-linking density and the similar chemical environment for reactive beads at different times and temperatures, the reaction equilibrium constant is $K_{\rm eq} = \frac{k^+}{k^-} = 1$ in eq 13, where k^+ and k^- are the forward and backward reaction rates, respectively. By contrast, for physical

Macromolecules Article pubs.acs.org/Macromolecules

associative polymer networks as described by Hoy and Fredrickson,⁴⁶ the cross-linking density or the number of dynamic bonds varies remarkably with temperature; thus, the corresponding reaction equilibrium constant $K_{\rm eq}$ is considerably affected by temperature instead of a constant. The reaction rates can be given according to the Arrhenius model

$$k^{+} = k^{-} = \nu \exp\left(-\frac{E_{\text{a,bs}}}{T}\right) \tag{15}$$

where the prefactor v is related to the MC time step and the probability p_{bs} of a dynamic bond and a free reactive bead within the reactive range (0.87 $\leq r \leq$ 1.14), and is given by $v = \frac{P_{\rm bs}}{\tau_{\rm MC}}$; $E_{\rm a,bs}$ is the activation energy of the bond exchange.

Thus, $\exp\left(-\frac{E_{a,bs}}{T}\right)$ can be regarded as the reaction probability that can be obtained by the simulation. We calculated the reaction probability at different temperatures, which is the ratio between the number of successful bond exchanges and attempted bond exchanges. As shown in Figure S1, they follow an Arrhenius-like equation and the corresponding activation energy $E_{a,bs} = 1.8$. Therefore, the rate of bond exchange is fast in our model vitrimeric system.

■ RESULTS AND DISCUSSION

Glass-Transition Temperatures and Topological Structure Change. The average volumes at different temperatures from T = 0.1-2.0 are collected to identify the glass-transition temperature T_g of the vitrimeric model system. As shown in Figure 2, $T_g = 0.4$ is determined by linearly fitting the volume data at low and high temperatures.

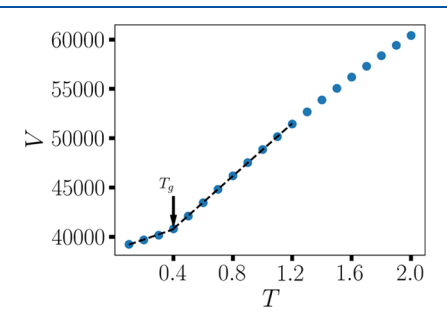


Figure 2. System average volume as a function of temperature T. The dashed lines are the linear fit to the volume data at low and high temperatures. The intersection point corresponds to the glasstransition temperature T_o .

Given that the model vitrimeric system is analogous to the real vulcanized network, we hypothesize that there are various topological structures or bonds, such as loop, bridge, and dangling, created by the cross-linkers. We first calculate the percent of these topological structures at different temperatures. As shown in Figure 3a, the average percentage of the total number of dynamic bonds $\langle p_{\text{total}} \rangle = \frac{\text{num}_{\text{total}}}{\text{num}_{B}}$, where num_{total} and num_B are, respectively, the total number of dynamic bonds and B beads, which actually corresponds to the system cross-linking density, is a constant of $\langle p_{\text{total}} \rangle = 1$ and does not change with temperature. Additionally, the average percent of dangling structures formed by the cross-linkers $\langle p_{\text{dangling}} \rangle = 0$ implies that all of the B beads in cross-linkers are involved in the reaction with A beads in the polymer chains.

Interestingly, as seen in the inset plots of Figure 3a, the percent of bridge (or loop) bonds increases (or decreases) slightly from $\langle p_{\text{bridge}} \rangle = 0.857 - 0.883$ (or $\langle p_{\text{loop}} \rangle = 0.143 - 0.115$) with decreasing temperature until entering the glassy state. Seeing that only the spare A beads in the main chain can trigger the bond-exchange reaction, we think this is probably due to the sluggish movement of polymer chains at a low temperature, leading to the decrease of the probability p_{bs} . However, it is noted that these changes are very small, as also supported by Figure 3b, which shows the probability distribution of the number of bridge and loop bonds in each polymer chain. We can find that these data points at different temperatures basically overlap each other. The distribution of bridge bonds can be well fitted by a Gaussian equation

$$P_{\text{bridge}} = 0.23 \exp\left(-0.5\left(\frac{n_{\text{bridge}} - 3.24}{1.74}\right)^2\right)$$
, which is due to the

fact that the reactive A beads are randomly grafted in the polymer chain. The corresponding mean value of the bridge bond number per chain is $\langle n_{\text{bridge}} \rangle = 3.24$, indicating that the polymer system is indeed a gelation network. The distribution of loop bonds can be well fitted by a Poisson function

$$P_{\mathrm{loop}} = \frac{\exp(-0.24)0.24^{(n_{\mathrm{loop}})}}{(n_{\mathrm{loop}})!}$$
, and the corresponding average

number of loop bonds per chain is $\langle n_{\text{loop}} \rangle = 0.24$. These simulated results suggest that the hybrid MD-MC simulation method successfully captures the bond-exchange mechanism and the topological structure variations with temperature in vitrimers, in good agreement with experiments.^{23,55}

Topological Freezing Transition Temperature and Microscopic Dynamics. To identify the topological freezing transition temperature T_{ν} of the model vitrimeric system, we calculate the autocorrelation functions of all of the dynamic bonds C_{total} , loop bonds C_{loop} , and bridge bonds C_{bridge} defined

$$C_{i} = \frac{\langle H(t+t_{0})H(t_{0})\rangle}{\langle H(t_{0})^{2}\rangle}$$
(16)

where $H(t_0)$ is the number of dynamic bonds at t_0 and H(t + t_0) is the number of surviving dynamic bonds still consisting of the same sticky beads over an interval of t. Additionally, we also compute the incoherent intermediate scattering function (ISF) $F_s(\mathbf{q}, t)$ of the reactive B beads commonly used to characterize the structural relaxation time on computer simulations, which is given by

$$F_{s}(\mathbf{q}, t) = N_{B}^{-1} \langle \sum_{i=1}^{N_{B}} \exp[i\mathbf{q} \cdot (\mathbf{r}_{i}(t) - \mathbf{r}_{i}(0))] \rangle$$
(17)

where N_B is the total number of reactive B beads and $\langle \cdot \rangle$ represents the time average. q is the wave vector, and its amplitude $|\mathbf{q}| = 1.4$ is adopted to compute $F_s(\mathbf{q}, t)$ at different temperatures, which approximately corresponds to the first peak position of the static structure factor of the B beads. The decay of these autocorrelation functions with time at various temperatures is shown in Figure S2. The corresponding lifetime or relaxation time τ_i , where i = total, loop, bridge, and F_s , is all defined as $C_i(\tau_i) = 0.3$ or $F_s(\mathbf{q}, \tau_{F_s}) = 0.3$. Figure 4 shows the relaxation time τ_i as a function of the inverse temperature 1/T. A similar method described by Perego et al. 32 is applied to determine T_{ν} , wherein the Arrhenius $\left(\tau_i = A \exp\left(\frac{E_a}{k_B T}\right)\right)$ and WLF $\left(\tau_i = A \exp\left(\frac{-C_1(T - T_0)}{C_2 + (T - T_0)}\right)\right)$

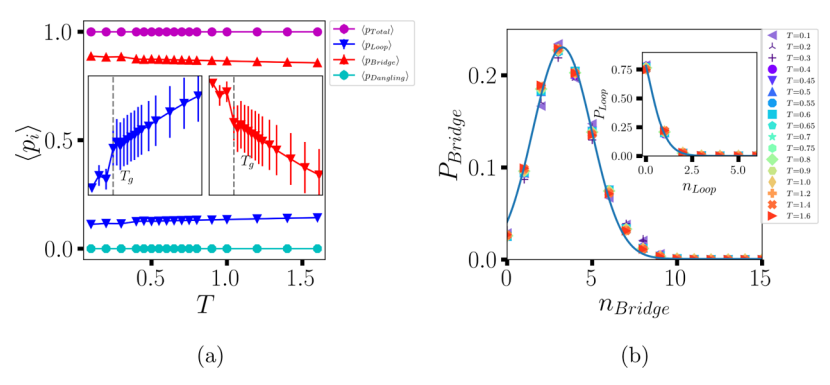


Figure 3. (a) Average percent of the total dynamic $\langle p_{\text{total}} \rangle$ and various topological bonds $(\langle p_{\text{loop}} \rangle, \langle p_{\text{bridge}} \rangle)$, and $\langle p_{\text{dangling}} \rangle)$ as a function of temperature T, where the inset plots are the enlarged plots for $\langle p_{\text{loop}} \rangle$ and $\langle p_{\text{bridge}} \rangle$. (b) Probability distribution of the number of bridge bonds in each polymer chain for various temperatures, and the solid curve is a Gaussian fit $P_{\text{bridge}} = 0.23 \exp \left(-0.5 \left(\frac{n_{\text{bridge}} - 3.24}{1.74}\right)^2\right)$. Inset: Probability distribution of the number of loop bonds in each polymer chain at different temperatures, and a Poisson function, $P_{\text{loop}} = \frac{\exp(-0.24)0.24^{(n_{\text{loop}})}}{(n_{\text{loop}})!}$, to fit the data is also shown by the solid curve.

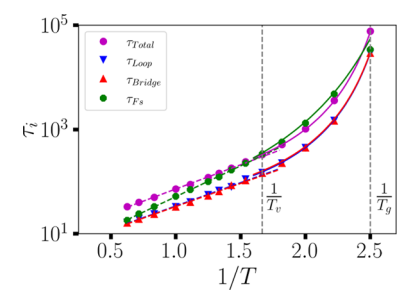


Figure 4. Microscopic dynamic relaxation time as a function of reciprocal temperature 1/T. τ_{total} , τ_{loop} , τ_{bridge} , and τ_{F_s} are the relaxation times of the autocorrelation functions of all of the dynamic bonds $C_{\text{total}}(t)$, loop bonds $C_{loops}(t)$, bridge bonds C_{bridges} , and incoherent intermediate scattering function of the reactive B beads $F_s(\mathbf{q}, t)$ with | q = 1.4, whose results are given in Figure S2. The vertical dashed lines stand for the positions of the inverse values of topological freezing (T_v) and glass-transition (T_o) temperatures. The dashed and solid lines are the Arrhenius and WLF fit to the data, respectively. The equations of these fitting curves are, respectively, $\tau_{\text{total}} = 8.49 \exp\left(\frac{2.14}{T}\right), \ \tau_{\text{loop}} = 4.37 \exp\left(\frac{2.05}{T}\right), \ \tau_{\text{bridge}} = 4.32 \exp\left(\frac{2.04}{T}\right)$, and $au_{F_s} = 3.4~{
m exp}{\left({\frac{{2.72}}{T}} \right)}$ for the purple, blue, red, and green dashed $\tau_{\text{total}} = 130005 \exp\left(\frac{-7.87(T - 0.395)}{0.065 + (T - 0.395)}\right)$
$$\begin{split} &\tau_{\text{loop}} = 109598 \, \exp\!\left(\frac{-8.41(T-0.389)}{0.059 + (T-0.389)}\right)\!, \\ &\tau_{\text{bridge}} = 111766 \, \exp\!\left(\frac{-8.38(T-0.389)}{0.059 + (T-0.389)}\right)\!, \end{split}$$
a n d $au_{F_{\rm s}} = 106330 \; {
m exp} igg(rac{-8.73 (T - 0.391)}{0.111 + (T - 0.391)} igg) \; \; {
m for \; \; the \; \; purple, \; \; blue, \; red, \; and}$ green solid lines.

equations are utilized to fit the relaxation time data at high and low temperatures, respectively, as depicted by the dashed and solid lines in Figure 4. Thereby, the same topological freezing transition temperature $T_{\nu}=0.6$ is determined from the dynamic bonds and ISF relaxation of the reactive B beads, which is 1.5 times the glass-transition temperature $T_{\rm g}=0.4$ (see Figure 2), consistent with Perego et al. The energy barrier $E_{\rm a}$ in the Arrhenius equation for the relaxation of all of the dynamic bonds is basically the same as those of the bridge and loop bonds, that is, $E_{\rm a}\approx 2.1$, but different from the one of

ISF relaxation $E_{\rm a}\approx 2.7$, which will be discussed further below. Additionally, it is worth mentioning that the relaxation time of bridge bonds is almost the same as the one of loop bonds, which is likely due to the short chain length of cross-linkers consisting of three beads considered in our simulated system.

The average ensemble behaviors of dynamic bonds have been studied above. To go further, we explore the dynamic behavior of single beads involved in the bond exchange, that is, the B beads. To this end, we calculated the reduced number of bond exchange n_{exchange} for each reactive B bead during a longtime interval $\Delta t_{\rm int} = 2.5 \times 10^5$ at various temperatures, $n_{\text{exchange}} = \frac{\text{num}_{\text{exchange}}}{\text{nframe}}$, where $\text{num}_{\text{exchange}}$ is the bond-exchange number and n_{frame} is the frame number of the collected configurations ($n_{\text{frame}} = 5000$ is considered in the calculation). The projections of the average snapshots of B beads in the zdirection are shown in Figures 5a and S3 at different temperatures, where the different color of each bead stands for the different values of $n_{\rm exchange}$. With temperature $T \leq T_{\nu}$ = 0.6, the bond-exchange behavior exhibits distinct dynamic heterogeneity, that is, the different reactive B beads have significantly different reduced numbers of bond exchanges. As further proven in Figure 5b, the probability distribution of n_{exchange} becomes wider with decreasing temperature. We also analyze the variation of its average value, $\langle n_{\text{exchange}} \rangle$, with temperature. As illustrated in the following plot of Figure 5b, we find that when $T \le T_{\nu\nu} \langle n_{\rm exchange} \rangle$ as a function of 1/T can be well fitted by an Arrhenius equation $\langle n_{\text{exchange}} \rangle = 3.52 \exp\left(\frac{-1.47}{T}\right)$. As $T > T_v$, they can be well described by a power-law equation of 1/T: $\langle n_{\text{exchange}} \rangle = T^{-0.5} +$ 1.01, which is obviously reasonable that $\langle n_{\text{exchange}} \rangle$ should be close to 1 at a high-enough temperature. It should be noted that $\langle n_{\text{exchange}} \rangle$ is affected by kinetics and thermodynamics, thus exhibiting a different temperature dependence from the reaction probability with decreasing temperature.

Furthermore, we also compute the non-Gaussian parameter $\alpha_2(t)$ at different temperatures usually used in glass-forming liquids⁵⁶ to characterize the dynamic heterogeneity of the vitrimeric system, which is defined by

$$\alpha_2(t) = 3\langle r^4(t)\rangle/5\langle r^2(t)\rangle^2 - 1 \tag{18}$$

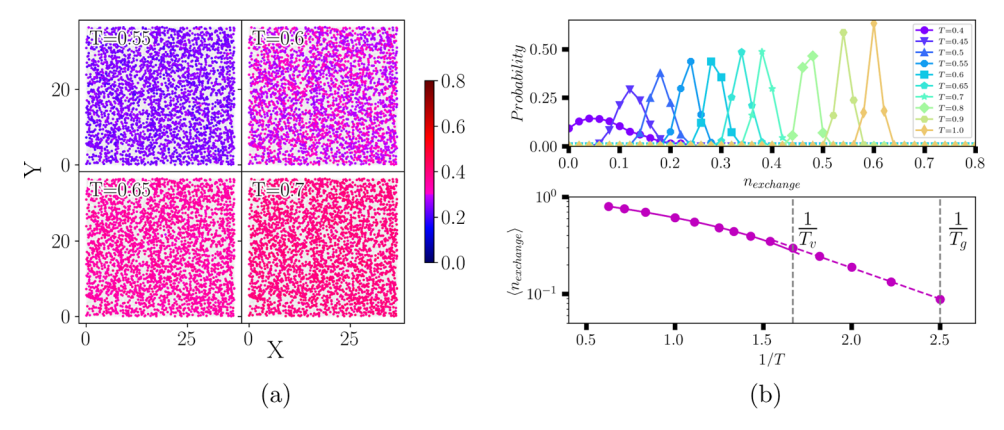


Figure 5. (a) Projections of the average snapshots of the reactive *B* beads in the *z* direction at several typical temperatures, where the different color of each bead stands for the different value of the reduced number of bond exchange n_{exchange} during a long-time interval $\Delta t_{\text{int}} = 2.5 \times 10^5$. (b) The above plot in (b) corresponds to the probability distribution of n_{exchange} and the following figure in (b) shows its average value $\langle n_{\text{exchange}} \rangle$ as a function of the reciprocal temperature 1/T, where the dashed and solid lines are the Arrhenius and power-law fits to the data: $\langle n_{\text{exchange}} \rangle = 3.52 \exp\left(\frac{-1.47}{T}\right)$ and $\langle n_{\text{exchange}} \rangle = T^{-0.5} + 1$.

where r(t) is the bead displacement during time t. The non-Gaussian parameter can reflect the degree of deviation from the homogeneous dynamics. The results are plotted in Figure 6. As with supercooled liquids, $\alpha_2(t)$ first increases with time

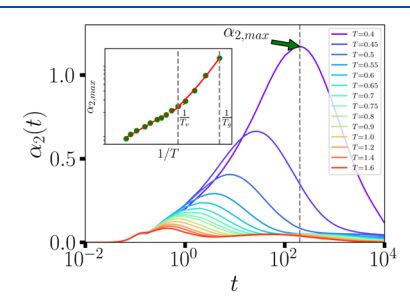
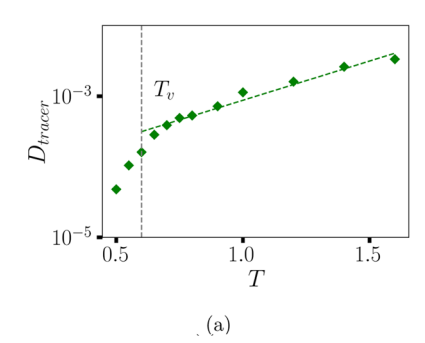


Figure 6. Non-Gaussian parameter $\alpha_2(t)$ as a function of time t at different temperatures, where the vertical dashed line corresponds to the maximum of $\alpha_2(t)$ at T=0.4. Inset: Variation of the maximum of the non-Gaussian parameter $\alpha_{2,\max}$ with the reciprocal temperature 1/T, where the dashed and solid lines are the Arrhenius and WLF fits to the dashed at a: $\alpha_{2,\max} = 0.049 \exp\left(\frac{0.942}{T}\right)$ and $\alpha_{2,\max} = 1.249 \exp\left(\frac{-3.673(T-0.396)}{0.248+T-0.396}\right)$.

and reaches a maximum $\alpha_{2,\text{max}}$, followed by a decay upon entering the free diffusive regime. Consequently, the maximum of the non-Gaussian parameter $\alpha_{2,\text{max}}$ is commonly used to evaluate the magnitude of dynamic heterogeneity. The inset plot of Figure 6 shows $\alpha_{2,\text{max}}$ as a function of the reciprocal temperature 1/T. As with the relaxation time of the dynamic bonds, the Arrhenius and WLF equations can also be separately used to describe the variation of $\alpha_{2,\text{max}}$ at high and low temperatures. Moreover, the same transition temperature, $T_{\nu}=0.6$, is also determined. Therefore, these simulated results suggest that the dynamic heterogeneity of the vitrimeric system will increase remarkably with temperatures lower than the topological freezing transition temperature.

Linear Rheology. With the purpose of describing the linear viscoelastic behavior of unentangled vitrimers by the SRM, Ricarte et al.³⁴ assumed that there were no unpaired reactive beads and that the bond exchange might only occur when two dynamic bonds were in a certain range; thus, the cross-linking positions did not change with time and temperature. However, for our vitrimeric model system and for most of the associative bond-exchange chemistries used in the literature, there must be some spare reactive beads in the polymer chain for performing the bond exchange. Therefore, the number and positions of sticky beads per chain always vary with time and temperature. Nevertheless, we determine below



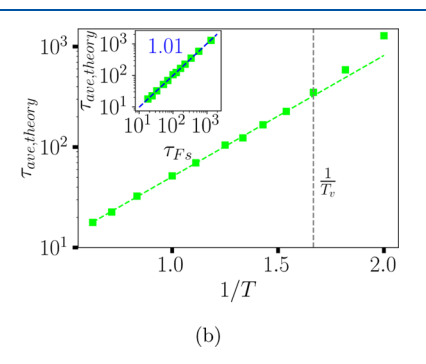


Figure 7. (a) Variation of the center-of-mass diffusion constant of the tracer chains D_{tracer} with temperature T, where the green dashed line corresponds to an Arrhenius fit: $D_{\text{tracer}} = 6.76 \times 10^{-5} \exp(2.56T)$. (b) Average relaxation time obtained by the SRM (see eq. 8) $\tau_{\text{ave,theory}}$ as a function of the reciprocal temperature 1/T, where the Arrhenius fit to the data is shown by the green dashed line: $\tau_{\text{ave,theory}} = 3.16 \exp\left(\frac{2.78}{T}\right)$. Inset: logarithm plot of $\tau_{\text{ave,theory}}$ and the relaxation time of ISF τ_{F_s} , and the dashed line is the linear fit, indicating that $\tau_{F_s} \propto \tau_{\text{ave,theory}}$.

whether the SRM can be used to predict the linear rheological behavior of the vitrimeric model system.

Determination of Parameters in the Sticky Rouse Model. As mentioned in the previous section, the relative effective frictional coefficient $\delta = \frac{\zeta}{\zeta}$ is one of the key parameters for predicting the linear rheological properties of unentangled vitrimers in terms of the SRM. Following the work of Jiang et al., 37 we identify the values of δ at different temperatures by calculating the chain center-of-mass diffusion constant $D_{\rm cm}$. In addition, considering the background friction (ζ) acting on the regular beads also changes with temperature and density, 57-59 we introduce five linear tracer chains with the same chain length of 46 as the matrix chains and without any reactive beads grafted in the polymer chain to the vitrimeric matrices. The background friction coefficient is also extracted from the center-of-mass diffusion constant D_{tracer} of the tracer chains, which corresponds to the slope of the time-dependent meansquared displacement (MSD) of the tracer chain center-ofmass as presented in Figure S4b. With D_{cm} and D_{tracer} , the relative effective frictional coefficient δ for the sticky beads can be directly obtained.³⁷

It should be noted that although the reactive A beads are randomly grafted in the polymer chain and the positions and number of sticky beads in each chain vary with time, the value of D_{cm} does not depend on the way of the definition of the chain center-of-mass and is not affected by the chain topological structures.³⁷ We analyze the variation of the tracer chain center-of-mass diffusion constant D_{tracer} with temperature, where the results at T = 0.45 and 0.40 are not shown in view of the very long simulation time we need to run for ensuring that the tracer chain center-of-mass diffusion reaches a Fick regime. As presented in Figure 7a, there is indeed a significant change in the background surrounding. With a decrease in temperature, the motion of the tracer chains is gradually suppressed, indicating that the system becomes viscous. There is a sharp change of $D_{\rm tracer}$ as the system approaches the topological freezing transition temperature T_v = 0.6, consistent with the variation of the microscopic dynamic relaxation and the non-Gaussian maximum $\alpha_{2,max}$ in Figures 4

The linear rheological properties of unentangled vitrimers can be directly predicted by the SRM based on these equations in the model section in conjunction with the simulated system parameters and some quantities identified above such as D_{cm} and D_{tracer} . Taking the average relaxation time as an example (see eq 8), the key quantity we need to calculate is the relaxation time spectrum $\tau_i = \frac{\tau_0}{2\lambda_i}$. For a specific chain conformation and distribution of the sticky beads, the eigenvalues (λ_i) of the connection matrix **A** can be identified based on the effective friction coefficient δ . According to the Einstein relation $\zeta = \frac{k_{\rm B}T}{{\rm ND}_{\rm tracer}}$ for a tracer chain, 37 τ_0 can also be expressed as $au_0 = rac{b^2}{3{
m ND}_{
m tracer}}$, where the Kuhn length $b = \sqrt{C_{\infty}} l$ with the characteristic ratio $C_{\infty} \approx 1.80$ and the average bond length $l \approx 0.96$ for our simulated system. Therefore, it is possible to predict the relaxation time and linear viscoelasticity of untangled vitrimers from the SRM without introducing any fitting parameters. Due to the different distribution of the reactive A beads in each polymer chain and the variation of the sticky bead positions with time, we need to analyze each chain, identify the sticky bead positions and topological structure, and

average the results over an ensemble of polymer chains. Figure 7b presents the change of the average relaxation time $\tau_{\text{ave,theory}}$ with temperature. An Arrhenius-like behavior is also found at $T > T_{\nu\nu}$ and the energy barrier obtained by fitting $E_{\text{a}} = 2.78$ is very close to the one in the relaxation time of ISF of the reactive B beads τ_{F_s} . Moreover, the values of $\tau_{\text{ave,theory}}$ are proportional to τ_{Fs} , that is, $\tau_{Fs} \propto \tau_{\text{ave,theory}}$, as illustrated in the inset plot of Figure 7b, indicating that the behavior of the segmental relaxation in unentangled vitrimers is successfully captured by the SRM and the parameters obtained above are in a reasonable range.

Comparison of the Simulation and the Sticky Rouse Model. In the equilibrium simulation, the linear stress relaxation modulus G(t) is computed by the time correlation functions of different components of the stress tensor $\sigma_{\alpha\beta}$ according to the Green–Kubo relationship

$$G(t) = \frac{V}{5k_{\rm B}T} [\langle \sigma_{xy}(t)\sigma_{xy}(0)\rangle + \langle \sigma_{yz}(t)\sigma_{yz}(0)\rangle + \langle \sigma_{zx}(t)\sigma_{zx}(0)\rangle] + \frac{V}{30k_{\rm B}T} [\langle N_{xy}(t)N_{xy}(0)\rangle + \langle N_{yz}(t)N_{yz}(0)\rangle + \langle N_{zx}(t)N_{zx}(0)\rangle]$$
(19)

where V is the system volume. $N_{\alpha\beta} = \sigma_{\alpha\alpha} - \sigma_{\beta\beta}$, which is the corresponding normal stress difference, is also considered for improving the accuracy of the results, and the multitau correlator algorithm⁶⁰ is applied to reduce the strong noise of these correlation functions. We run a long-enough simulation time that is several orders of magnitude larger than the longest relaxation time and three different initial configurations to obtain an accurate G(t). A new effective tool, that is, i-Rheo GT,61 has been proposed to correctly educe the frequencydependent complex modulus from the time-dependent shear modulus by means of direct Fourier transformation without discarding the fluctuations related to the bond relaxation and widely applied in numerical simulations. 62,63 To obtain the continuous change of the dynamic modulus with frequency ω , the i-Rheo GT tool is utilized to calculate the elastic/storage $G'(\omega)$, loss $G'(\omega)$ moduli, and viscosity $\eta(\omega)$ by the direct analytical transformation of the raw data on G(t) shown in Figures S5a-c and S6a. The oscillations at the short time in Figure S5a are related to the bond relaxation commonly observed in the KGBS model.⁶⁴ At low temperatures, a plateau emerges in the stress relaxation and elastic moduli due to the glassy behavior. The loss modulus goes through a maximum and decreases gradually with decreasing frequency. At long time or low frequency, these moduli all decrease approaching the terminal relaxation due to the bond exchange, showing a liquid-like behavior, in line with the experimental results. 16,30,33

Apart from the linear relaxation moduli, the SRM can also predict the motion of segments.³⁷ For the convenience of comparison between the SRM predictions and the simulated results, we calculate the MSD of a segment relative to the chain effective center-of-mass, which is defined as

$$g_2(t) = \langle [(\mathbf{r}_i(t) - \mathbf{r}_{\text{cm/eff}}(t)) - (\mathbf{r}_i(0) - \mathbf{r}_{\text{cm/eff}}(0))]^2 \rangle$$
(20)

where $\mathbf{r}_{\text{cm/eff}}(t) = \sum_{i=1}^{i=N} \zeta_i \mathbf{R}_i / \sum_{i=1}^{N} \zeta_i$ is the effective center-of-mass of a chain at t containing the friction coefficients of beads. Given that the number and positions of the sticky beads in each polymer chain vary with time and temperature, it is

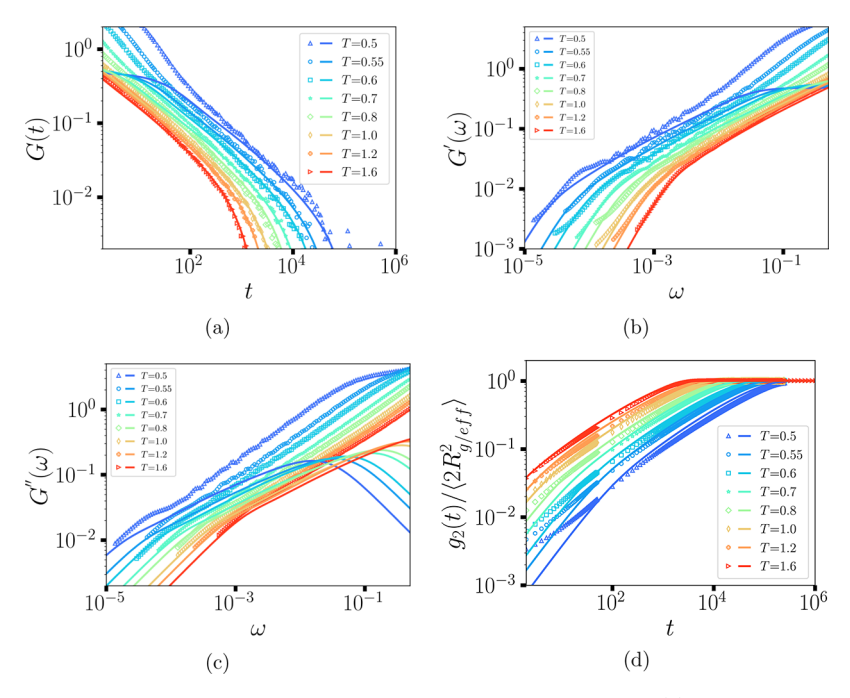


Figure 8. Comparison between the simulated results and the theoretical values of the SRM for (a) the stress relaxation modulus G(t), (b) the elastic modulus $G'(\omega)$, (c) the loss modulus $G''(\omega)$, and (d) the reduced mean-squared displacement of segments relative to the effective mass center of a chain $g_2(t)/(2R_{g/eff}^2)$ at different temperatures, where the symbols are the simulation results and the solid lines are the predicted values of the SRM by analyzing each chain without introducing any fitting parameters. The results for the other temperatures are shown in Figure S7.

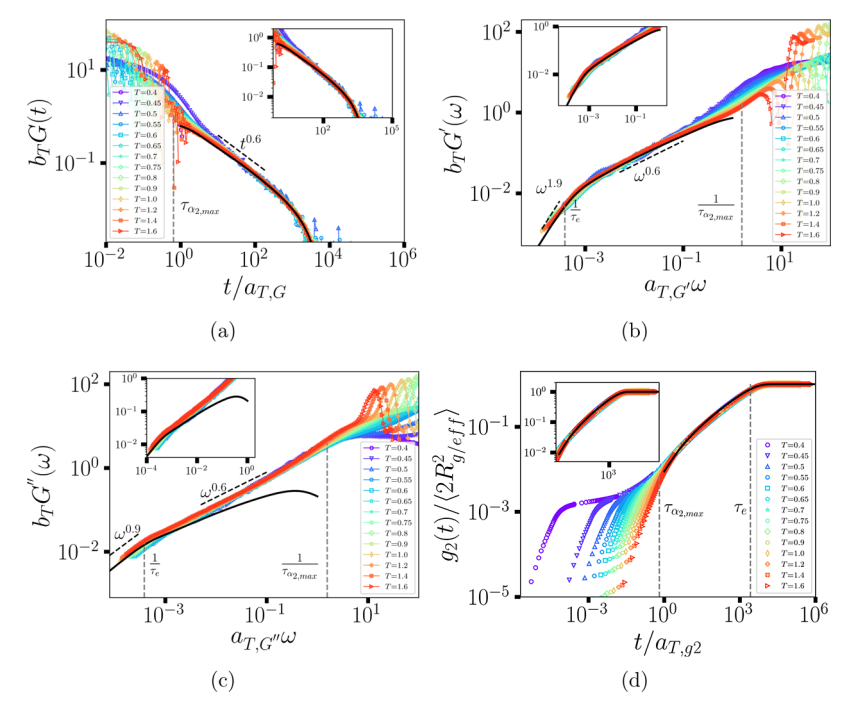


Figure 9. Rescaled (a) stress relaxation G(t), (b) elastic $G'(\omega)$ and (c) loss $G''(\omega)$ moduli, and (d) the mean square displacement of segments relative to the effective mass center of a chain $g_2(t)/\langle 2R_{g'eff}^2\rangle$ as a function of the reduced time or frequency at different temperatures. The black solid lines are the SRM predictions at the reference temperature $T_{ref}=1.0$ based on eqs 4, 5, 6, and 20. Inset: Corresponding results at the intermediate and long time or low frequencies.

difficult to identify the effective chain center-of-mass in our simulations. Due to the small energy barrier of bond exchange considered ($E_{\rm a,bs}=1.8$), the definition of the chain effective center-of-mass should have a small influence on the simulated results of $g_2(t)$. As a result, the chain effective center-of-mass is defined as $\mathbf{r}_{\rm cm/eff}(t) = \sum_{i=1}^{i=N} \mathbf{R}_i / \sum_{i=1}^{N} i$ in all of the simulation

lations. Figure S5 shows the reduced $g_2(t)$ at different temperatures, where $\langle R_{\rm g/eff}^2 \rangle$ is the effective mean-squared radius of gyration. At the long-time limit, $g_2(t)$ should approach a plateau value of $\langle 2R_{\rm g/eff}^2 \rangle$ according to its definition (see eq 20). Consequently, the rescaled ultimate value of $g_2(t \to +\infty)$ should be 1, as supported in Figure S5d.

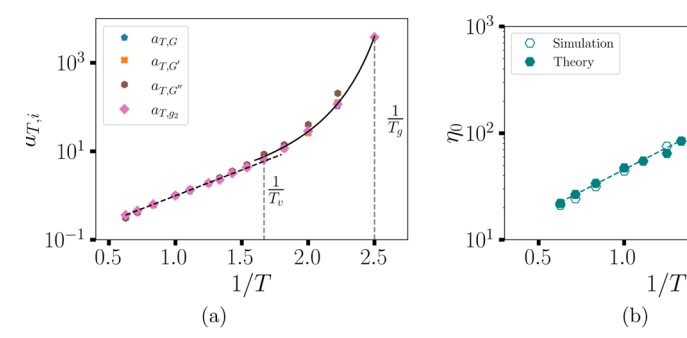


Figure 10. (a) Horizontal shift factors $a_{T,G}$, a $a_{T,G'}$, and a_{T,g_2} used to collapse the moduli and relative mean square displacement data versus 1/T, where the fitting equations of the Arrhenius and WLF are, respectively, $a_{T,i} = 0.067 \exp\left(\frac{2.69}{T}\right)$ for the dashed line and $a_{T,i} = 56602 \exp\left(\frac{-11.16(T-0.383)}{0.0545+(T-0.383)}\right)$ for the solid line. (b) Zero-shear viscosity η_0 as a function of reciprocal temperature 1/T, where the empty symbols are the simulation results and the solid symbols are the SRM predicted values obtained by calculating eq 7. The Arrhenius fitting equation is $\eta_0 = 6.92 \exp\left(\frac{1.9}{T}\right)$.

Based on the parameters identified in the previous section, the linear rheology and the segmental motion of the vitrimeric system should be described by the SRM. Figure 8 shows the comparison between the simulated results and the predicted values of the SRM without introducing any fitting parameters, where the part related to the bond relaxation is not presented for more clarity. A quantitative agreement is observed in these moduli and relative MSD of segments, especially at the medium and long times or low frequencies. For the vitrimeric melt at high temperatures such as T = 1.6, as depicted in Figure 8a,b,d, it is observed that the simulation results are basically in agreement with the theoretical predictions, implying that all of the assumptions in the SRM are satisfied by the simulation systems. With decreasing temperature, the glassy behavior will become more significant. As shown in Figure S5d, the duration of the cage regime formed by the nearest neighboring beads increases, which is commonly difficult to be captured by the SRM.⁶⁴ The corresponding Rouse regime, where there is a scaling of $t^{-0.5}$ before the terminal relaxation, shifts to a larger time or lower frequency scale. Although not so perfect as the predictions at high temperature, considerable agreement is still found between the simulation results and the theoretical curves at long time and low frequency. Given the quantitative agreement between theory and simulations found here and in the physical associative polymers studied previously,³⁷ we conclude that the associative mechanism has little effect on the effectiveness of the SRM in describing the linear viscoelasticity of associative polymer networks.

Furthermore, we examine the rationality of the time—temperature superposition (TTS) principle for our vitrimeric system. A reference temperature of $T_{\rm ref}=1.0$ is chosen. We first rescale the moduli by a vertical shift factor $b_T=T_{\rm ref}\rho_{\rm ref}/T\rho$, where $\rho_{\rm ref}$ and ρ are, respectively, the number density at $T_{\rm ref}$ and T. Then, the time and frequency are rescaled by a horizontal shift factor $a_{T,i}$, that is, $a_{T,G}$, $a_{T,G'}$, $a_{T,G''}$, and $a_{T,g,y}$ to shift the b_TG , b_TG' , b_TG'' , and $g_2/\langle 2R_{\rm g/eff}^2\rangle$ at different temperatures to the corresponding values at the reference temperature. The rescaled curves are shown in Figure 9. As mentioned in the previous section, the cage effect will become stronger with decreasing temperature, leading to the different relaxation behavior or mode at a short time 65 for various temperatures. As a result, they cannot collapse into a single

curve in a short time or high frequency. Similar results are observed in the theoretical results of the SRM34 and supercooled polymer melts.65 Considering that the non-Gaussian maximum $\alpha_{2,max}$ is related to the motion of particles in a cage, we approximately regard the time when the non-Gaussian $\alpha_2(t)$ reaches the corresponding maximum as the one when the particle escapes from the cage. As illustrated in the inset plots of Figure 9, with $t/a_{T,i} > \tau_{\alpha_2,\max}$ or $a_{T,i}\omega < 1/\tau_{\alpha_2,\max}$ these reduced values at different temperatures are basically collapsed onto a master curve. At the intermediate frequency or time, the moduli decrease gradually with the power law. The power-law exponent is about 0.6 in accordance with the one in the time-dependent MSD of the polymer chains (see Figure S4c), corresponding to the Rouse relaxation of segments. With frequency approaching the terminal relaxation time τ_e determined by calculating the autocorrelation function of chain ends (see Figure S6b), the elastic and loss moduli, respectively, follow $G' \propto \omega^{1.9}$ and $G' \propto \omega^{0.9}$, in good agreement with the predictions of the SRM.³⁴ The change of the power-law exponent from 0.6 to 1.9 in the reduced elastic modulus can be approximately considered as the transition of the rubberlike state to the viscous liquid. However, due to the fast bond exchange, the rubbery plateau is reduced to a narrow shoulder-like regime. Such a transition can be more clearly observed in the reduced relative MSD $g_2/\langle 2R_{g/eff}^2 \rangle$. As shown in Figure 8d, as $t > \tau_e$, $g_2/\langle 2R_{\rm g/eff}^2 \rangle$ is close to the plateau value, implying the system enters a viscous liquid state. Moreover, the overlap parts are quantitatively in good agreement with the SRM predictions at $T_{\text{ref}} = 1.0$ for $b_T G$, $b_T G'$, and $g_2 / \langle 2R_{g/\text{eff}}^2 \rangle$. Although the relaxation behavior of the reduced loss modulus b_TG'' at the intermediate frequency is not well reproduced by the SRM, its terminal relaxation is correctly predicted by the

2.0

1.5

These horizontal shift factors $a_{T,G}$, $a_{T,G'}$, $a_{T,G''}$, and a_{T,g_2} correspond to the ratios of the relaxation time at T to those at T_{ref} . Their values are plotted together in Figure 10 as a function of 1/T. An Arrhenius-type behavior is also observed at high temperatures with an energy barrier $E_a = 2.69$. At low temperatures, the WLF equation can describe well their variation with temperature. Besides being in good agreement with the temperature dependence of the dynamic bond and ISF relaxation and the non-Gaussian maximum $\alpha_{2,\text{max}}$, we also obtain the same transition temperature $T_{\nu} = 0.6$. Similar

behaviors are observed in the recent simulations and experiments of vitrimers. 30,31,48

The shear viscosity as a function of frequency at different temperatures can also be obtained by the i-Rheo GT tool, as presented in Figure S6a. With the decrease in frequency, the shear viscosity goes to a plateau value. Therefore, the corresponding zero-shear viscosity η_0 can be determined by extrapolating the shear viscosity to zero frequency. According to eq 7, the theoretical values of the zero-shear viscosity are also identified by the SRM model in terms of the parameters obtained in the previous section. These results are shown in Figure 10b. The SRM predictions almost perfectly match the simulated results. Moreover, the simulation and theoretical values both exhibit an Arrhenius-like behavior at $T > T_{\nu} = 0.6$, that is, $\eta_0 = 6.92 \exp\left(\frac{1.9}{T}\right)$, where the energy barrier $E_a = 1.9$ is very close to the one obtained by fitting for the relaxation time of the dynamic bonds ($E_a = 2.1$; see Figure 4). As indicated in previous works, 16,31,32 compared to the permanent polymer networks, the dynamic cross-links in vitrimers accelerate the segmental relaxation and lead to an Arrhenius-like behavior, in agreement with our simulated results.

Discussion. Based on the results obtained above, we can find that when approaching T_{ν} , there are significant transitions in the microscopic dynamics and macroscopic rheological behaviors, as suggested in Figures 4, 5, 6, and 10. To determine if there is a gelation-like transition in proximity to T_{ν} as found in DCANs,²⁰ we plot the loss and elastic moduli near $T_{\nu} = 0.6$ together in Figure 11. Interestingly, a similar frequency scaling

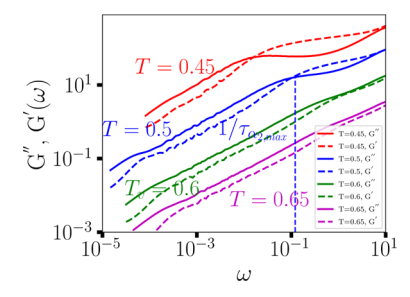


Figure 11. Variation of the elastic $G'(\omega)$ (dashed lines) and loss $G''(\omega)$ (solid lines) moduli with frequency ω at several typical temperatures $T=0.45,\ 0.5,\ 0.6$, and 0.65. The vertical blue dashed line represents the position of the inverse value of $\tau_{\alpha_2,\max}$ at T=0.5, very close to the intersection point between the elastic and loss moduli, which suggests that i-Rheo GT is indeed an effective tool. To reduce visual clutter, the curves at T=0.45 and T=0.5 are shifted up by one and two decades and the curve at T=0.65 is shifted down by one decade.

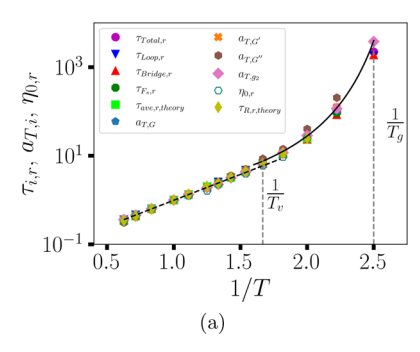
is observed in the loss and elastic moduli at $T = T_w$ reminiscent of the gelation transition discussed in the introduction section. However, it occurs in the regime with high frequencies larger than the dynamic bond relaxation time $1/\tau_{\rm total}$; thus, it cannot be considered a gelation-like transition based on the Winter—Chambon gel-point criterion. ²² As indicated by the vertical blue dashed line in Figure 11, the position of the intersection point between the elastic and loss moduli is close to the inverse value of $\tau_{\alpha_2, {\rm max}}$. Thus, the occurrence of such a crossover at high frequencies should be related to the glassy behavior. As discussed in the previous section, the duration of the cage regime increases with the decrease of temperature (see Figure S5d). The corresponding frequency regime where the elastic

modulus is larger than the loss modulus also expands, as shown in Figure 11. According to Larini et al., ⁶⁶ the structural relaxation time is related to the short time vibrational dynamics for glass-forming liquids and polymers. Consequently, we can think that the cage effect starts to emerge on approaching T_{ν} , which affects not only the dynamic behavior at relatively short times such as non-Gaussian maximum $\alpha_{2,\max}$ but also the intermediate and long-time relaxation dynamics, such as the dynamic bond relaxation, the horizontal shift factor, and the zero-shear viscosity.

Additionally, we find that the microscopic and macroscopic relaxation dynamics exhibit a similar temperature dependence; that is, the Arrhenius and WLF equations can be used to describe the corresponding relaxation behaviors at temperatures lower and higher than T_{v} , respectively. However, different from the horizontal shift factor, the average relaxation time of the SRM, and τ_F , the zero-shear viscosity and the dynamic bond relaxation show a smaller energy barrier Ea in the Arrhenius fitting equations (see Figures 5 and 10). This is mainly because the effects of temperature and density are taken into account in the definition of these quantities (eq 7). Therefore, a method similar to the TTS principle is adopted to rescale the zero-shear viscosity and the dynamic bond relaxation time by the vertical shift factor, that is, $b_T \eta_0$, $b_T \tau_{\text{total}}$, $b_T \tau_{\text{loop}}$, and $b_T \tau_{\text{bridge}}$. To derive a master curve, the rescaled quantities, the average relaxation time, and τ_{F_c} at different temperatures are reduced by the values at the reference temperature $T_{ref} = 1$. A scaling collapse curve is obtained in Figure 12a without introducing any fitting parameters, where the dashed and solid curves are the fitting equations determined in the horizontal shift factor $a_{T,i}$ (see Figure 10) and the Rouse relaxation time $\tau_{\rm R,theory}$ derived from the SRM is also included in the plot. Furthermore, these reduced quantities are plotted together as a function of the reduced relaxation time of dynamic bonds and follow a linear relationship. Consequently, these results suggest that the microscopic and macroscopic dynamics exhibit a similar relaxation behavior for our model vitrimeric system with a lower barrier although there exist some topological defects.

CONCLUSIONS

In summary, a hybrid MD-MC simulation method is applied to investigate the topological structure change, dynamic heterogeneity, and linear rheological properties of unentangled sidechain-linked vitrimers in combination with the sticky Rouse model (SRM). We find that there is a minor variation in topological structures with temperature (see Figure 3), consistent with the experiments.⁵⁵ By analyzing the relaxation time of the dynamic bonds, various topological bonds, and the incoherent intermediate scattering function (ISF) of the reactive B beads $(F_s(\mathbf{q}, t))$, we determine the same topological freezing transition temperature T_{ν} = 0.6, as shown in Figure 4. With temperature approaching T_{ν} , the bond-exchange behavior and the system dynamics both show significant dynamic heterogeneity; the latter increases following a combination of Arrhenius and WLF-like behaviors (see Figures 5 and 6). To examine the effectiveness and validity of the SRM in predicting the linear rheology of our model vitrimeric system, where the number and positions of sticky beads in each polymer chain vary with time and temperature, the relative efficient friction coefficient δ is obtained by calculating the center-of-mass diffusion constants of the matrix and tracer chains. Various



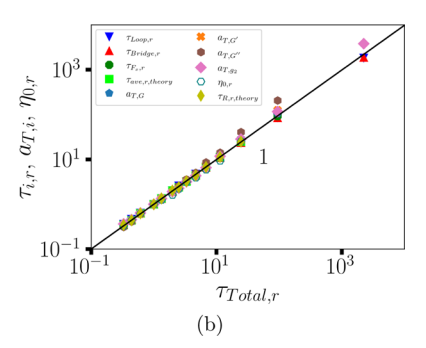


Figure 12. (a) Master curve of various rescaled microscopic and macroscopic relaxation quantities as a function of the reciprocal temperature 1/T. The dashed and solid lines are the Arrhenius and WLF fits to the data, respectively. (b) Various rescaled microscopic and macroscopic relaxation quantities versus the reduced relaxation time of the dynamic bonds τ_{total} , where $\tau_{R,r, \text{theory}}$ is the reduced Rouse relaxation time obtained by the SRM. $\tau_{E,r} = \frac{\tau_{E_g}(T)}{\tau_{E_g}(T_{\text{ref}})}$, $\tau_{\text{ave,theory}} = \frac{\tau_{\text{ave,theory}}(T)}{\tau_{\text{ave,theory}}}$, $\tau_{\text{R,r,theory}} = \frac{\tau_{\text{R,theory}}(T)}{\tau_{\text{R,theory}}}$, $\tau_{\text{total}}(T_{\text{ref}})$, $\tau_{\text{loop,r}} = \frac{b_T \tau_{\text{loop}}(T)}{\tau_{\text{loop}}(T_{\text{ref}})}$, $\tau_{\text{bridge}}(T_{\text{ref}})$, and $\eta_{0,r} = \frac{b_T \eta_{\text{loof}}(T)}{\eta_{\text{o}}(T_{\text{ref}})}$.

relaxation moduli and the diffusive behavior of segments relative to the chain center-of-mass are predicted without introducing any parameters based on the values of δ . A quantitative agreement between the simulation and theoretical results is observed for the relaxation of the shear modulus G(t), the elastic modulus $G'(\omega)$, and the reduced MSD relative to the chain center-of-mass $g_2/\langle 2R_{\rm g/eff}^2\rangle$, especially at the intermediate and long time or low frequency. Additionally, the terminal relaxation of loss modulus $G''(\omega)$ is also quantitatively predicted by the SRM (see Figure 8). The time—temperature superposition (TSS) principle is examined by shifting these rescaled moduli and $g_2/\langle 2R_{\rm g/eff}^2\rangle$ to the corresponding values at the reference temperature. We find the TTS principle is only satisfied at $t/a_{T,i} > \tau_{\alpha_2,\max}$ or $a_{T,i}\omega < 1/2$

The black solid line in (b) is a linear fitting to the data

 $au_{a_2,\mathrm{max}}$ in line with the predictions of the SRM. ³⁴ By analyzing the variation of the shift factors with temperature, we obtain the same topological freezing transition temperature with relaxation of dynamic bonds and ISF of the reactive beads B. Moreover, the simulated results and the SRM predictions of the zero-shear viscosity both follow an Arrhenius-like behavior at $T > T_{\nu}$, and their values are quantitatively consistent (see Figure 10). A method similar to the TTS principle is adopted to rescale the relaxation time of various dynamic bonds and zero-shear viscosity by using the vertical shift factor b_T . A scaling collapse curve is obtained for various relaxation quantities, including the zero-shear viscosity, the Rouse relaxation time, and the horizontal shift factors. Therefore, our simulated results suggest that the microscopic and macroscopic dynamics exhibit a similar relaxation behavior for unentangled vitrimers with a low energy barrier although there exist some topological defects, which are correctly captured by the SRM.

The SRM was originally proposed for the transient polymer network connected by physical interactions, and its validity has been proved for physical associative polymers.³⁷ From our investigated results, SRM can also correctly describe the microscopic dynamic relaxation and macroscopic linear rheological properties for unentangled vitrimers with a low energy barrier. This indicates that the effectiveness and validity of the SRM are independent of the associative mechanism. The linear viscoelastic behaviors of associative polymers are correctly predicted via a single-chain approach, especially for the polymer system with a low sticky energy. In future simulations, we will further study the effect of the energy

barrier of bond exchange and the cross-linker concentration on the dynamics and rheology of unentangled vitrimers.

ASSOCIATED CONTENT

Supporting Information

Supporting Information contains one file with The Supporting Information is available free of charge at https://pubs.acs.org/doi/10.1021/acs.macromol.3c01366.

Reaction probability; microscopic dynamic relaxation; average snapshots of reactive beads; mean square displacement; temperature dependence of moduli and mean square displacement relative to the chain center-of-mass; viscosity and relaxation of chain ends; comparison between the predictions of the sticky Rouse model and simulated results (PDF)

AUTHOR INFORMATION

Corresponding Author

Monica Olvera de la Cruz — Department of Materials Science and Engineering, Northwestern University, Evanston, Illinois 60208, United States; Department of Chemistry, Department of Chemical and Biological Engineering, and Department of Physics and Astronomy, Northwestern University, Evanston, Illinois 60208, United States; orcid.org/0000-0002-9802-3627; Email: m-olvera@northwestern.edu

Authors

Jianshe Xia — Department of Materials Science and Engineering, Northwestern University, Evanston, Illinois 60208, United States; orcid.org/0000-0002-5120-4885

Julia Ann Kalow — Department of Chemistry, Northwestern University, Evanston, Illinois 60208, United States; orcid.org/0000-0002-4449-9566

Complete contact information is available at: https://pubs.acs.org/10.1021/acs.macromol.3c01366

Notes

The authors declare no competing financial interest.

ACKNOWLEDGMENTS

The work was funded by the NSF Center for the Chemistry of Molecularly Optimized Networks (MONET), CHE-2116298. M.O.d.l.C. and J.X. thank the support of the Center for Computation and Theory of Soft Materials.

REFERENCES

- (1) Biron, M. Thermoplastics and Thermoplastic Composites: Technical Information for Plastics Users; Elsevier, 2007.
- (2) Morales Ibarra, R. Thermosets, 2nd ed.; Guo, Q., Ed.; Elsevier, 2018; pp 639-666.
- (3) Utekar, S.; VK, S.; More, N.; Rao, A. Comprehensive study of recycling of thermosetting polymer composites Driving force, challenges and methods. *Composites, Part B* **2021**, 207, 108596.
- (4) Campanella, A.; Döhler, D.; Binder, W. H. Self-Healing in Supramolecular Polymers. *Macromol. Rapid Commun.* **2018**, 39, No. 1700739.
- (5) Cordier, P.; Tournilhac, F.; Soulié-Ziakovic, C.; Leibler, L. Selfhealing and thermoreversible rubber from supramolecular assembly. *Nature* **2008**, *451*, 977–980.
- (6) Fox, J. D.; Rowan, S. J. Supramolecular Polymerizations and Main-Chain Supramolecular Polymers. *Macromolecules* **2009**, 42, 6823–6835.
- (7) Burnworth, M.; Tang, L.; Kumpfer, J. R.; Duncan, A. J.; Beyer, F. L.; Fiore, G. L.; Rowan, S. J.; Weder, C. Optically healable supramolecular polymers. *Nature* **2011**, *472*, 334–337.
- (8) Liu, K.; Kang, Y.; Wang, Z.; Zhang, X. 25th Anniversary Article: Reversible and Adaptive Functional Supramolecular Materials: "Noncovalent Interaction" Matters. *Adv. Mater.* **2013**, *25*, 5530–5548.
- (9) Lewis, C. L.; Dell, E. M. A review of shape memory polymers bearing reversible binding groups. *J. Polym. Sci., Part B: Polym. Phys.* **2016**, *54*, 1340–1364.
- (10) Wu, S.; Chen, Q. Advances and New Opportunities in the Rheology of Physically and Chemically Reversible Polymers. *Macromolecules* **2022**, *55*, 697–714.
- (11) Scheutz, G. M.; Lessard, J. J.; Sims, M. B.; Sumerlin, B. S. Adaptable Crosslinks in Polymeric Materials: Resolving the Intersection of Thermoplastics and Thermosets. *J. Am. Chem. Soc.* **2019**, *141*, 16181–16196.
- (12) Kloxin, C. J.; Bowman, C. N. Covalent adaptable networks: smart, reconfigurable and responsive network systems. *Chem. Soc. Rev.* **2013**, *42*, 7161–7173.
- (13) Zhang, V.; Kang, B.; Accardo, J. V.; Kalow, J. A. Structure-Reactivity-Property Relationships in Covalent Adaptable Networks. *J. Am. Chem. Soc.* **2022**, *144*, 22358–22377.
- (14) Porath, L.; Soman, B.; Jing, B. B.; Evans, C. M. Vitrimers: Using Dynamic Associative Bonds to Control Viscoelasticity, Assembly, and Functionality in Polymer Networks. *ACS Macro Lett.* **2022**, *11*, 475–482
- (15) Samanta, S.; Kim, S.; Saito, T.; Sokolov, A. P. Polymers with Dynamic Bonds: Adaptive Functional Materials for a Sustainable Future. *J. Phys. Chem. B* **2021**, *125*, 9389–9401.
- (16) Montarnal, D.; Capelot, M.; Tournilhac, F.; Leibler, L. Silica-Like Malleable Materials from Permanent Organic Networks. *Science* **2011**, 334, 965–968.
- (17) Webber, M. J.; Tibbitt, M. W. Dynamic and reconfigurable materials from reversible network interactions. *Nat. Rev. Mater.* **2022**, 7, 541–556.
- (18) Krishnakumar, B.; Sanka, R. P.; Binder, W. H.; Parthasarthy, V.; Rana, S.; Karak, N. Vitrimers: Associative dynamic covalent adaptive networks in thermoset polymers. *Chem. Eng. J.* **2020**, 385, 123820.
- (19) Van Zee, N. J.; Nicolaÿ, R. Vitrimers: Permanently crosslinked polymers with dynamic network topology. *Prog. Polym. Sci.* **2020**, *104*, No. 101233.
- (20) Adzima, B. J.; Aguirre, H. A.; Kloxin, C. J.; Scott, T. F.; Bowman, C. N. Rheological and Chemical Analysis of Reverse Gelation in a Covalently Cross-Linked Diels-Alder Polymer Network. *Macromolecules* **2008**, *41*, 9112–9117.
- (21) Bergman, S. D.; Wudl, F. Mendable polymers. *J. Mater. Chem.* **2008**, *18*, 41–62.
- (22) Winter, H. H. Can the gel point of a cross-linking polymer be detected by the G'-G" crossover? *Polym. Eng. Sci.* **1987**, 27, 1698–1702.

- (23) Chakma, P.; Konkolewicz, D. Dynamic Covalent Bonds in Polymeric Materials. *Angew. Chem., Int. Ed.* **2019**, *58*, 9682–9695.
- (24) Zheng, J.; Png, Z. M.; Ng, S. H.; Tham, G. X.; Ye, E.; Goh, S. S.; Loh, X. J.; Li, Z. Vitrimers: Current research trends and their emerging applications. *Mater. Today* **2021**, *51*, 586–625.
- (25) Ishibashi, J. S. A.; Kalow, J. A. Vitrimeric Silicone Elastomers Enabled by Dynamic Meldrum's Acid-Derived Cross-Links. *ACS Macro Lett.* **2018**, *7*, 482–486.
- (26) El-Zaatari, B. M.; Ishibashi, J. S. A.; Kalow, J. A. Cross-linker control of vitrimer flow. *Polym. Chem.* **2020**, *11*, 5339–5345.
- (27) Denissen, W.; Winne, J. M.; Du Prez, F. E. Vitrimers: permanent organic networks with glass-like fluidity. *Chem. Sci.* **2016**, 7, 30–38.
- (28) Nishimura, Y.; Chung, J.; Muradyan, H.; Guan, Z. Silyl Ether as a Robust and Thermally Stable Dynamic Covalent Motif for Malleable Polymer Design. *J. Am. Chem. Soc.* **2017**, *139*, 14881–14884.
- (29) Guerre, M.; Taplan, C.; Winne, J. M.; Du Prez, F. E. Vitrimers: directing chemical reactivity to control material properties. *Chem. Sci.* **2020**, *11*, 4855–4870.
- (30) Fang, H.; Ye, W.; Ding, Y.; Winter, H. H. Rheology of the Critical Transition State of an Epoxy Vitrimer. *Macromolecules* **2020**, 53, 4855–4862.
- (31) Perego, A.; Khabaz, F. Volumetric and Rheological Properties of Vitrimers: A Hybrid Molecular Dynamics and Monte Carlo Simulation Study. *Macromolecules* **2020**, *53*, 8406–8416.
- (32) Perego, A.; Lazarenko, D.; Cloitre, M.; Khabaz, F. Microscopic Dynamics and Viscoelasticity of Vitrimers. *Macromolecules* **2022**, *55*, 7605–7613.
- (33) Meng, F.; Saed, M. O.; Terentjev, E. M. Rheology of vitrimers. *Nat. Commun.* **2022**, *13*, No. 5753.
- (34) Ricarte, R. G.; Shanbhag, S. Unentangled Vitrimer Melts: Interplay between Chain Relaxation and Cross-link Exchange Controls Linear Rheology. *Macromolecules* **2021**, *54*, 3304–3320.
- (35) Cui, X.; Jiang, N.; Shao, J.; Zhang, H.; Yang, Y.; Tang, P. Linear and Nonlinear Viscoelasticities of Dissociative and Associative Covalent Adaptable Networks: Discrepancies and Limits. *Macromolecules* **2023**, *56*, 772–784.
- (36) Jiang, N.; Zhang, H.; Tang, P.; Yang, Y. Linear Viscoelasticity of Associative Polymers: Sticky Rouse Model and the Role of Bridges. *Macromolecules* **2020**, *53*, 3438–3451.
- (37) Jiang, N.; Zhang, H.; Yang, Y.; Tang, P. Molecular dynamics simulation of associative polymers: Understanding linear viscoelasticity from the sticky Rouse model. *J. Rheol.* **2021**, *65*, 527–547.
- (38) Sciortino, F. Three-body potential for simulating bond swaps in molecular dynamics. *Eur. Phys. J. E* **2017**, *40*, No. 3, DOI: 10.1140/epje/i2017-11496-5.
- (39) Rovigatti, L.; Nava, G.; Bellini, T.; Sciortino, F. Self-Dynamics and Collective Swap-Driven Dynamics in a Particle Model for Vitrimers. *Macromolecules* **2018**, *51*, 1232–1241.
- (40) Ciarella, S.; Sciortino, F.; Ellenbroek, W. G. Dynamics of Vitrimers: Defects as a Highway to Stress Relaxation. *Phys. Rev. Lett.* **2018**, *121*, 058003.
- (41) Ciarella, S.; Biezemans, R. A.; Janssen, L. M. C. Understanding, predicting, and tuning the fragility of vitrimeric polymers. *Proc. Natl. Acad. Sci. U.S.A.* **2019**, *116*, 25013–25022.
- (42) Ciarella, S.; Ellenbroek, W. Swap-Driven Self-Adhesion and Healing of Vitrimers. *Coatings* **2019**, *9*, 114.
- (43) Zhao, H.; Wei, X.; Fang, Y.; Gao, K.; Yue, T.; Zhang, L.; Ganesan, V.; Meng, F.; Liu, J. Molecular Dynamics Simulation of the Structural, Mechanical, and Reprocessing Properties of Vitrimers Based on a Dynamic Covalent Polymer Network. *Macromolecules* **2022**, *55*, 1091–1103.
- (44) Wu, J.-B.; Li, S.-J.; Liu, H.; Qian, H.-J.; Lu, Z.-Y. Dynamics and reaction kinetics of coarse-grained bulk vitrimers: a molecular dynamics study. *Phys. Chem. Chem. Phys.* **2019**, *21*, 13258–13267.
- (45) Amin, D.; Likhtman, A. E.; Wang, Z. Dynamics in Supramolecular Polymer Networks Formed by Associating Telechelic Chains. *Macromolecules* **2016**, *49*, 7510–7524.

- (46) Hoy, R. S.; Fredrickson, G. H. Thermoreversible associating polymer networks. I. Interplay of thermodynamics, chemical kinetics, and polymer physics. *J. Chem. Phys.* **2009**, *131*, No. 224902.
- (47) Wilson, M.; Rabinovitch, A.; Baljon, A. R. C. Computational Study of the Structure and Rheological Properties of Self-Associating Polymer Networks. *Macromolecules* **2015**, *48*, *6313–6320*.
- (48) Perego, A.; Khabaz, F. Effect of bond exchange rate on dynamics and mechanics of vitrimers. *J. Polym. Sci.* **2021**, *59*, 2590–2602.
- (49) Kremer, K.; Grest, G. S. Dynamics of entangled linear polymer melts: A molecular-dynamics simulation. *J. Chem. Phys.* **1990**, 92, 5057–5086.
- (50) Pütz, M.; Kremer, K.; Grest, G. S. What is the entanglement length in a polymer melt? *Europhys. Lett.* **2000**, *49*, 735.
- (51) Grest, G. S.; Kremer, K. Statistical properties of random cross-linked rubbers. *Macromolecules* **1990**, 23, 4994–5000.
- (52) Everaers, R.; Sukumaran, S. K.; Grest, G. S.; Svaneborg, C.; Sivasubramanian, A.; Kremer, K. Rheology and Microscopic Topology of Entangled Polymeric Liquids. *Science* **2004**, *303*, 823–826.
- (53) Hoy, R. S.; Foteinopoulou, K.; Kröger, M. Topological analysis of polymeric melts: Chain-length effects and fast-converging estimators for entanglement length. *Phys. Rev. E* **2009**, *80*, No. 031803.
- (54) Plimpton, S. Fast Parallel Algorithms for Short-Range Molecular Dynamics. *J. Comput. Phys.* **1995**, *117*, 1–19.
- (55) Porath, L. E.; Evans, C. M. Importance of Broad Temperature Windows and Multiple Rheological Approaches for Probing Viscoelasticity and Entropic Elasticity in Vitrimers. *Macromolecules* **2021**, *54*, 4782–4791.
- (56) Xia, J.; Guo, H. Construction of a quantitative relation between structural relaxation and dynamic heterogeneity by vibrational dynamics in glass-forming liquids and polymers. *Soft Matter* **2021**, 17, 10753–10764.
- (57) von Meerwall, E. D.; Lin, H.; Mattice, W. L. Trace Diffusion of Alkanes in Polyethylene: Spin-Echo Experiment and Monte Carlo Simulation. *Macromolecules* **2007**, *40*, 2002–2007.
- (58) von Meerwall, E.; Feick, E. J.; Ozisik, R.; Mattice, W. L. Diffusion in binary liquid n-alkane and alkane-polyethylene blends. *J. Chem. Phys.* **1999**, *111*, 750–757.
- (59) von Meerwall, E.; Beckman, S.; Jang, J.; Mattice, W. L. Diffusion of liquid n-alkanes: Free-volume and density effects. *J. Chem. Phys.* **1998**, *108*, 4299–4304.
- (60) Ramírez, J.; Sukumaran, S. K.; Vorselaars, B.; Likhtman, A. E. Efficient on the fly calculation of time correlation functions in computer simulations. *J. Chem. Phys.* **2010**, *133*, No. 154103, DOI: 10.1063/1.3491098.
- (61) Tassieri, M.; Ramírez, J.; Karayiannis, N. C.; Sukumaran, S. K.; Masubuchi, Y.; i-Rheo, G. T. Transforming from Time to Frequency Domain without Artifacts. *Macromolecules* **2018**, *51*, 5055–5068.
- (62) Huang, L.-H.; Hua, C.-C. Predictive Mesoscale Simulation of Flow-Induced Blend Morphology, Interfacial Relaxation, and Linear Viscoelasticity of Polymer-Elastomer Blends. *Macromolecules* **2022**, *55*, 7353–7367.
- (63) Behbahani, A. F.; Schneider, L.; Rissanou, A.; Chazirakis, A.; Bačová, P.; Jana, P. K.; Li, W.; Doxastakis, M.; Polińska, P.; Burkhart, C.; Müller, M.; Harmandaris, V. A. Dynamics and Rheology of Polymer Melts via Hierarchical Atomistic, Coarse-Grained, and Slip-Spring Simulations. *Macromolecules* **2021**, *54*, 2740–2762.
- (64) Likhtman, A. E.; Sukumaran, S. K.; Ramirez, J. Linear Viscoelasticity from Molecular Dynamics Simulation of Entangled Polymers. *Macromolecules* **2007**, *40*, 6748–6757.
- (65) Pan, D.; Sun, Z.-Y. Diffusion and Relaxation Dynamics of Supercooled Polymer Melts. Chin. J. Polym. Sci. 2018, 36, 1187–1194.
- (66) Larini, L.; Ottochian, A.; De Michele, C.; Leporini, D. Universal scaling between structural relaxation and vibrational dynamics in glass-forming liquids and polymers. *Nat. Phys.* **2008**, *4*, 42–45.